nanomaterials

MDPI

Article

Influence of Grain Boundary Scattering on the Field-Effect Mobility of Solid-Phase Crystallized Hydrogenated Polycrystalline In_2O_3 (In_2O_3:H)

Yusaku Magari [1,*], Wenchang Yeh [1], Toshiaki Ina [2] and Mamoru Furuta [3]

[1] Graduate School of Natural Science and Technology, Shimane University, 1060 Nishikawatsu, Matsue 690-8504, Japan
[2] Japan Synchrotron Radiation Research Institute (JASRI/SPring-8), 1-1-1 Kouto, Sayo 679-5198, Japan
[3] School of Environmental Science and Engineering and Research Institute, Kochi University of Technology, 185 Miyanokuchi, Tosayamada, Kami 782-8502, Japan
* Correspondence: magari.yusaku@riko.shimane-u.ac.jp; Tel.: +81-852-32-8903

Abstract: Hydrogenated polycrystalline In_2O_3 (In_2O_3:H) thin-film transistors (TFTs) fabricated via the low-temperature solid-phase crystallization (SPC) process with a field-effect mobility (μ_{FE}) exceeding 100 $cm^2\ V^{-1}\ s^{-1}$ are promising candidates for future electronics applications. In this study, we investigated the effects of the SPC temperature of Ar + O_2 + H_2-sputtered In_2O_3:H films on the electron transport properties of In_2O_3:H TFTs. The In_2O_3:H TFT with an SPC temperature of 300 °C exhibited the best performance, having the largest μ_{FE} of 139.2 $cm^2\ V^{-1}\ s^{-1}$. In contrast, the μ_{FE} was slightly degraded with increasing SPC temperature (400 °C and higher). Extended X-ray absorption fine structure analysis revealed that the medium-range ordering in the In_2O_3:H network was further improved by annealing up to 600 °C, while a large amount of H_2O was desorbed from the In_2O_3:H films at SPC temperatures above 400 °C, resulting in the creation of defects at grain boundaries. The threshold temperature of H_2O desorption corresponded well with the carrier transport properties; the μ_{FE} of the TFTs started to deteriorate at SPC temperatures of 400 °C and higher. Thus, it was suggested that the hydrogen remaining in the film after SPC plays an important role in the passivation of electron traps, especially for grain boundaries, resulting in an enhancement of the μ_{FE} of In_2O_3:H TFTs.

Keywords: polycrystalline oxide semiconductors; In_2O_3:H; solid-phase crystallization; thin-film transistors; high mobility

Citation: Magari, Y.; Yeh, W.; Ina, T.; Furuta, M. Influence of Grain Boundary Scattering on the Field-Effect Mobility of Solid-Phase Crystallized Hydrogenated Polycrystalline In_2O_3 (In_2O_3:H). *Nanomaterials* **2022**, *12*, 2958. https://doi.org/10.3390/nano12172958

Academic Editor: Béla Pécz

Received: 15 July 2022
Accepted: 24 August 2022
Published: 26 August 2022

1. Introduction

Amorphous oxide semiconductors (AOSs), represented by amorphous In–Ga–Zn–O (a-IGZO), have now become standard channel materials in thin-film transistors (TFTs) for active-matrix liquid-crystal displays and active-matrix organic light-emitting diode displays [1–3]. This is because a-IGZO has properties that are superior to hydrogenated amorphous Si (a-Si:H), such as a large field-effect mobility (μ_{FE}) of over 10 $cm^2\ V^{-1}\ s^{-1}$, an extremely low leakage current, a low processing temperature (<350 °C), and excellent uniformity [4–12]. Although the μ_{FE} value of a-IGZO TFTs is more than ten times higher than that of a-Si:H TFTs (<1 $cm^2\ V^{-1}\ s^{-1}$), the further improvement of μ_{FE} values is required to expand their range of applications as alternatives to poly-Si TFTs (50–100 $cm^2\ V^{-1}\ s^{-1}$) [13]. The optimization of AOS composition is one approach for improving μ_{FE}; for example, an increase in the In ratio due the considerable spatial spread of the In 5*s* orbital with a large overlap can provide a facile electron transport path with a low electron effective mass [14,15]. Although various compositions, including In–Sn–Zn–O [16,17], In–W–Zn–O [18,19], Al–In–Sn–Zn–O [20], and In–Ga–Zn–Sn–O [21], have been proposed to enhance the μ_{FE}, the value remains insufficiently high to compete with that of low-temperature polysilicon (LTPS) TFTs [22].

In contrast, the crystallization of OSs is an another approach for improving μ_{FE}, because the subgap density of states originating from structural disorder and defects can be suppressed via lattice ordering. Although polycrystalline Oss, including In_2O_3, ZnO, and SnO_2, have been investigated as channel materials in early oxide-based TFTs [23–25], they can easily create oxygen vacancies, leading to degenerate semiconductors. In addition, μ_{FE} degradation due to grain boundary scattering is a serious issue for polycrystalline OSs as well as poly-Si [26,27]. Polycrystalline In_2O_3 films have been investigated for use as the transparent conductive oxide (TCO) in solar cells. Koida et al. reported a degenerate hydrogen-doped polycrystalline In_2O_3 (In_2O_3:H) film with high electron mobility (100–130 $cm^2\ V^{-1}\ s^{-1}$) produced by solid-phase crystallization (SPC) [28]. Recently, we reported a μ_{FE} value of 139.2 $cm^2\ V^{-1}\ s^{-1}$ for a TFT obtained using hydrogenated polycrystalline In_2O_3 (In_2O_3:H) formed via SPC at 300 °C [29]. The obtained μ_{FE} value is comparable to the Hall mobility of single-crystalline epitaxial In_2O_3 films (~160 $cm^2\ V^{-1}\ s^{-1}$) [30]. The as-deposited amorphous In_2O_3:H was converted into a polycrystalline film with lateral grain sizes of about 140 nm via SPC [29]. However, the effects of SPC temperature on the electrical and structural properties of In_2O_3:H films are not yet understood in detail.

In this study, we investigated the effects of SPC temperature on electron transport properties in In_2O_3:H films and TFTs. Hydrogen intentionally doped during sputtering was found to play an essential role in the passivation of defects, especially for the grain boundaries of the films, resulting in an enhanced μ_{FE} of the TFTs.

2. Materials and Methods

2.1. Fabrication of In_2O_3:H TFTs

In_2O_3:H TFTs were fabricated on a heavily doped *p*-type Si substrate with a 100 nm thick thermally grown SiO_2 layer. The doped *p*-type Si substrate and SiO_2 layer were used as the gate electrode and gate insulator, respectively. The 30 nm thick In_2O_3:H channels were deposited via pulsed direct current (DC) magnetron sputtering, without substrate heating, from a ceramic In_2O_3 target using a mixture of Ar, O_2, and H_2 gases. The gas flow ratios of O_2 ($R[O_2] = O_2/(Ar + O_2 + H_2)$) and H_2 ($R[H_2] = H_2/(Ar + O_2 + H_2)$) were 1% and 5%, respectively. The deposition pressure and DC power were maintained at 0.6 Pa and 50 W, respectively. The base pressure before gas introduction was below 6×10^{-5} Pa. After deposition, the In_2O_3:H films were annealed in ambient air at a temperature range of 200–600 °C for 1 h. After annealing, a 100 nm thick SiO_2 film was deposited via reactive sputtering without substrate heating. Subsequently, Al source/drain electrodes were deposited via sputtering. Finally, the In_2O_3:H TFTs were annealed at 250 °C in ambient air for 1 h. In_2O_3:H, SiO_2, and Al films were deposited through a shadow mask, and both the channel length and width were 300 μm.

2.2. Characterization Methods

The carrier concentration (N_e) and Hall mobility (μ_{FE}) of the In_2O_3:H films were determined by Hall effect measurements (Accent, HL5500PC) using the van der Pauw geometry at room temperature. The local structural changes of the films were evaluated through extended X-ray absorption fine structure (EXAFS) at the BL01B1 beamline in SPring-8. The In K-edge fluorescence XAFS of the films was measured using a 19-element Ge detector with an incident X-ray angle of 2° with respect to the sample surface. The XAFS data were analyzed using the Demeter software packages [31]. The macroscopic structure of the In_2O_3:H films was observed using electron backscattering diffraction (EBSD) (EDAX-TSL Hikari High-Speed EBSD Detector). The hydrogen concentration in the films was measured using secondary ion mass spectrometry (SIMS) (ULVAC-PHI, ADEPT-1010) with Cs^+ as a primary ion. The chemical bonding states of the constituent elements and hydrogen were evaluated from their thermal effusion using thermal desorption spectroscopy (TDS), which was carried out while varying the stage temperature from 50 to 800 °C at a heating rate of 60 °C min^{-1}. Reference films of In_2O_3 under similar conditions maintaining an $R[H_2]$ of 0% (without hydrogen introduction) were deposited for comparison.

3. Results and Discussion

3.1. Electrical Properties of In_2O_3:H Films

Figure 1a shows the variations in N_e and μ_H in the 50 nm thick In_2O_3:H films as a function of the annealing temperature (T_{ann}). The N_e of the as-deposited film (5.7×10^{20} cm^{-3}) began to decrease rapidly from T_{ann} = 200 °C, where SPC occurred. Then, the In_2O_3:H exhibited an almost constant N_e of ~2×10^{17} cm^{-3} (an appropriate value for TFT fabrication) over a T_{ann} range of 300–500 °C. After reaching a T_{ann} of 600 °C, the N_e slightly increased to 1.4×10^{18} cm^{-3}. The μ_H of In_2O_3:H increased to 78.6 cm^2 V^{-1} s^{-1} after SPC occurred (T_{ann} = 200 °C), whereas the μ_H of the films decreased to ~15 cm^2 V^{-1} s^{-1} at a T_{ann} range of 250–350 °C. As T_{ann} further increased, the μ_H of In_2O_3:H began to decrease, resulting in a μ_H of 0.4 cm^2 V^{-1} s^{-1} at T_{ann} = 600 °C.

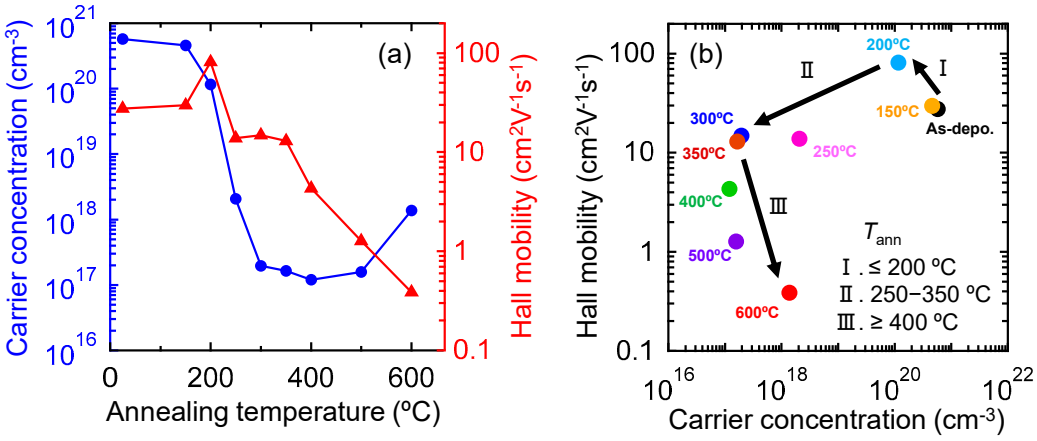

Figure 1. (**a**) N_e and μ_H of In_2O_3:H films as a function of T_{ann}. (**b**) Relationship between μ_H and N_e for In_2O_3:H films with various T_{ann} values.

To understand the carrier transport properties of the In_2O_3:H films, the relationship between μ_H and N_e for the films with various T_{ann} values is shown in Figure 1b. The changes in electrical properties could be classified into the following three regions: (I) enhanced μ_H at a $T_{ann} \leq 200$ °C; (II) decreased μ_H with decreasing N_e at T_{ann} = 250–350 °C; and (III) decreased μ_H with constant or increasing N_e at $T_{ann} \geq 400$ °C. The decrease in the μ_H of the polycrystalline In_2O_3:H films with increasing T_{ann} in regions II and III was considered to be due to the effects of grain boundary scattering and intragrain scattering. In general, for degenerate transparent conducting oxide materials, the mobility in the grains is determined by an optical method using the Drude model, because optical mobilities are not affected by grain boundary scattering [32,33]. However, it is difficult to determine the optical mobility of In_2O_3:H films annealed at $T_{ann} \geq 250$ °C because the free electrons are significantly decreased to the order of 10^{17} cm^{-3} and the films become non-degenerate semiconductors [34,35]. Therefore, we evaluated the effects of intragrain scattering by measuring the field-effect mobility of In_2O_3:H TFTs. This is because when a voltage is applied to the gate, a large number of carriers (10^{19}–10^{20} cm^{-3}) are accumulated at the In_2O_3:H/gate insulator interface, and the effects of grain boundary scattering can almost be neglected since electrons tunnel through the narrow width (<1 nm) of the grain barriers at high N_e values [36].

3.2. Electrical Properties of In_2O_3:H TFTs

Figure 2 shows the typical characteristics of the In_2O_3:H TFTs annealed at T_{ann} values of 200–600 °C. The μ_{FE} was calculated from the linear transfer characteristics (V_{ds} = 0.1 V) using the following equation:

$$\mu_{FE} = \frac{Lg_m}{WC_{ox}V_{ds}}$$

where g_m is the transconductance, C_{ox} is the oxide capacitance of the gate insulator, and V_{ds} is the drain voltage. V_{th} was defined by gate voltage (V_{gs}) at a drain current (I_{ds}) of 1 nA, and *SS* was extracted from V_{gs}, which required an increase in the I_{ds} from 10 to 100 pA. The average values and standard deviations (σ) of the characteristics of five TFTs on the same substrate are shown in Supplementary Figure S1 and Supplementary Table S1. The In_2O_3:H TFT annealed at 200 °C did not exhibit any switching (conductive behavior) because the In_2O_3:H film was still in a degenerated state ($N_e = 5.7 \times 10^{20}$ cm^{-3}). The TFTs annealed at 300 °C exhibited the best performance, with the largest field-effect mobility (μ_{FE}) of 139.2 cm^2 V^{-1} s^{-1} and smallest subthreshold swing (*SS*) of 0.19 Vdec^{-1} with an appropriate threshold voltage (V_{th}) of 0.2 V (shown in Figure 2c,e). Although the μ_H of the In_2O_3:H films decreased to 14.9 cm^2 V^{-1} s^{-1} with a N_e of 2.0×10^{17} cm^{-3} after annealing at 300 °C, as shown in Figure 1, extremely high μ_{FE} values were obtained from the TFTs at higher gate voltages (Figure 2b). Thus, we concluded that the decrease in μ_H in region II shown in Figure 1b) was mainly due to an increase in the potential barrier at the grain boundary caused by a decrease in N_e, rather than a decrease in intragrain mobility. In contrast, the TFT characteristics were slightly degraded when T_{ann} was increased to 600 °C, i.e., the μ_{FE} decreased and the *SS* value increased. Comparing μ_H and μ_{FE} after T_{ann} = 600 °C, the μ_H significantly deteriorated to 0.4 cm^2 V^{-1} s^{-1}, whereas the μ_{FE} of the TFTs was maintained at 94.6 cm^2 V^{-1} s^{-1}. This result suggests that grain boundary scattering is a dominant factor that limits the μ_H in films annealed at 400 °C and higher.

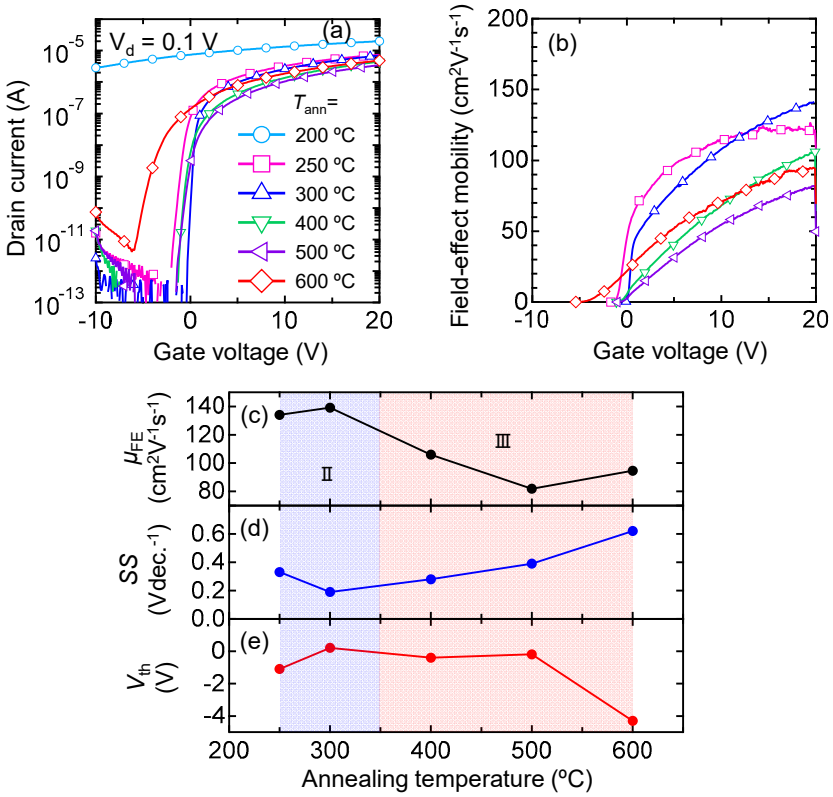

Figure 2. (**a**) Transfer characteristics and (**b**) μ_{FE} of the In_2O_3:H TFTs with channels annealed at various temperatures; T_{ann} dependence of (**c**) μ_{FE}, (**d**) *SS*, and (**e**) V_{th} in the In_2O_3:H TFTs.

3.3. Structural Properties of In_2O_3:H Films

To investigate the crystallinity of the films, the effect of T_{ann} on the local structure of the In_2O_3:H films was evaluated using XAFS. Figure 3 shows Fourier-transformed (FT) EXAFS spectra of the In K-edge for the (a) In_2O_3 and (b) In_2O_3:H films as a function of the phase uncorrected interatomic distance. The as-deposited In_2O_3 film without hydrogen introduction during sputtering exhibited three obvious peaks (Figure 3a), which corresponded to the nearest oxygen (In–O) and the second and third nearest In (In–In

and In–In*). Using the values for the crystalline In_2O_3 powder standard, the interatomic distance (R) and Debye–Waller factor (σ^2) for the films were determined. The k-range of the EXAFS data used in the analyses was k = 3–14 Å^{-1} with a k-weight of 3. The fitting carried out in the R space was from R = 1.0–4.0 Å for the three-shell model. As shown in Table 1, the $R_{In–O}$, $R_{In–In}$, and $R_{In–In*}$ values of the as-deposited In_2O_3 film without hydrogen were 2.16, 3.35, and 3.82 Å, respectively, which agreed well with the interatomic distance of the In_2O_3 bixbyite structure (space group Ia3, number 206) [37–39]. When the In_2O_3 film was annealed at 300 °C, no noticeable changes in R were observed (Figure 3a), while the peak intensity increased in each spectrum, resulting in a decrease in σ^2. This result indicates that thermal annealing improved the structural disorder of the films. By introducing hydrogen during sputtering, the second and third nearest peaks disappeared in the as-deposited In_2O_3:H film, while the intensity of the first nearest peak decreased (Figure 3b), resulting in an increase in $\sigma^2_{In–O}$ to 0.0112. In contrast, after annealing at 200 °C, the intensities of all peaks increased significantly and the intensities of the second and third nearest peaks were higher than those of the In_2O_3 film annealed at 300 °C. These results indicate that medium-range ordering was lost around In in the initial In_2O_3:H film, whereas medium-range ordering at distances equal to or longer than the second neighbor significantly improved after annealing at 200 °C. This is in agreement with a previous study using electron backscatter diffraction which confirmed that the amorphous state of the initial In_2O_3:H film and the grain size of the In_2O_3:H film were enlarged through SPC [29]. Therefore, the increase in μ_H after annealing at 200 °C, as shown in Figure 1b) (region I), is due to an increase in grain size as well as the improvement of the local structural order of the In_2O_3:H films. As T_{ann} increased from 200 to 300 °C, the intensity of the first nearest peak was constant, while the intensities of the second and third nearest peaks increased slightly, resulting in a decrease in $\sigma^2_{In–In}$ (0.0056) and $\sigma^2_{In–In}$ (0.0049). This result indicates that the medium-range ordering was improved by annealing at 300 °C, which is in good agreement with the high intragrain mobility obtained via μ_{FE} for the In_2O_3:H TFT annealed at 300 °C. As T_{ann} increased from 300 to 600 °C, the intensities of the second and third nearest peaks further increased, whereas R remained almost constant. Despite the improvement in the crystallinity of the In_2O_3:H films observed when annealing at 600 °C, the μ_{FE} of the TFTs slightly decreased to 94.6 cm^2 V^{-1} s^{-1}, as shown in Figure 2c, and the μ_H significantly deteriorated to 0.4 cm^2 V^{-1} s^{-1}. The deterioration of the μ_H of the In_2O_3:H films (Figure 1b, Region III) and the μ_{FE} of the TFTs annealed at ≥400 °C could not be explained by local structural changes in the In_2O_3:H films. Thus, it was suggested that the decreases in the μ_H and the μ_{FE} of the TFTs in region III shown in Figures 1b and 2c were mainly due to the formation of defects at grain boundaries.

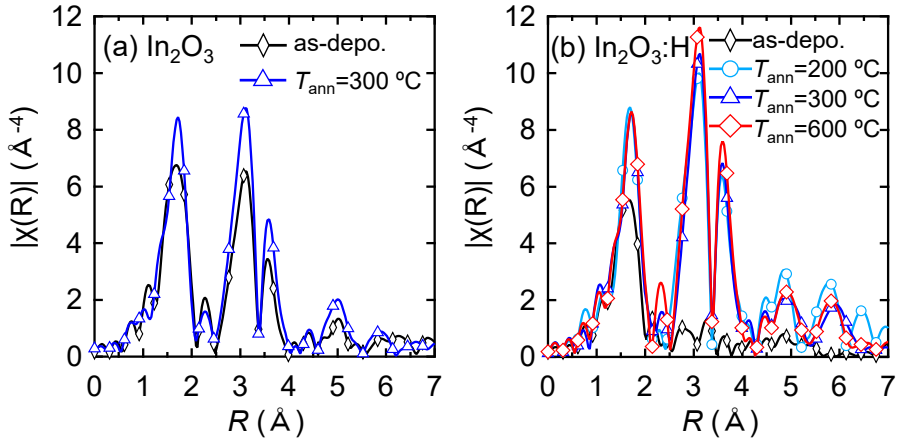

Figure 3. FT EXAFS spectra of the In K-edge for the (**a**) In_2O_3 and (**b**) In_2O_3:H films with various T_{ann} values.

Table 1. EXAFS fitting results for first, second, and third shells in the In_2O_3 and In_2O_3:H films.

		1st Shell (In–O)		2nd Shell (In–In)		3rd Shell (In–In*)	
	T_{ann} (°C)	R_{In-O} (Å)	σ^2_{In-O} (Å^2)	R_{In-In} (Å)	σ^2_{In-In} (Å^2)	R_{In-In^*} (Å)	$\sigma^2_{In-In^*}$ (Å^2)
In_2O_3	as-depo.	2.16	0.0090	3.35	0.0065	3.82	0.0066
In_2O_3	300	2.16	0.0073	3.36	0.0062	3.83	0.0063
In_2O_3:H	as-depo.	2.13	0.0112	-	-	-	-
In_2O_3:H	200	2.16	0.0072	3.36	0.0059	3.83	0.0051
In_2O_3:H	300	2.17	0.0072	3.36	0.0056	3.84	0.0049
In_2O_3:H	600	2.17	0.0072	3.37	0.0051	3.84	0.0046

To investigate the origin of the deterioration of the μ_H of In_2O_3:H films at $T_{ann} \geq 400$ °C, we performed EBSD measurements. Figure 4a–e depicts the EBSD images along the normal direction for the In_2O_3:H films with various T_{ann} values. The as-deposited amorphous In_2O_3:H film was converted into a polycrystalline In_2O_3:H film with grain structure embedded in the amorphous matrix at a T_{ann} of 150 °C (Figure 4b). At a T_{ann} of 200 °C (Figure 4c), the film was fully crystallized with a grain size of around 200 nm. After that, no significant difference was observed in the crystal grain size with increasing T_{ann} values up to 600 °C. The corresponding area fractions of the crystalline phase are shown in Figure 4f. All films showed a maximum area fraction for a grain size of ~200 nm; however, a small proportion of the area fraction with a grain size of ~15 nm was increased in the In_2O_3:H film annealed at 600 °C, as shown in the insets of Figure 4f. Moreover, these small domains were located in between the large grains, as shown in Figure 4e. The results indicate that when the In_2O_3:H films were annealed at 400 °C and higher, small domains were created at grain boundaries that served as electron traps, resulting in a decrease in the μ_H in region III shown in Figure 1b.

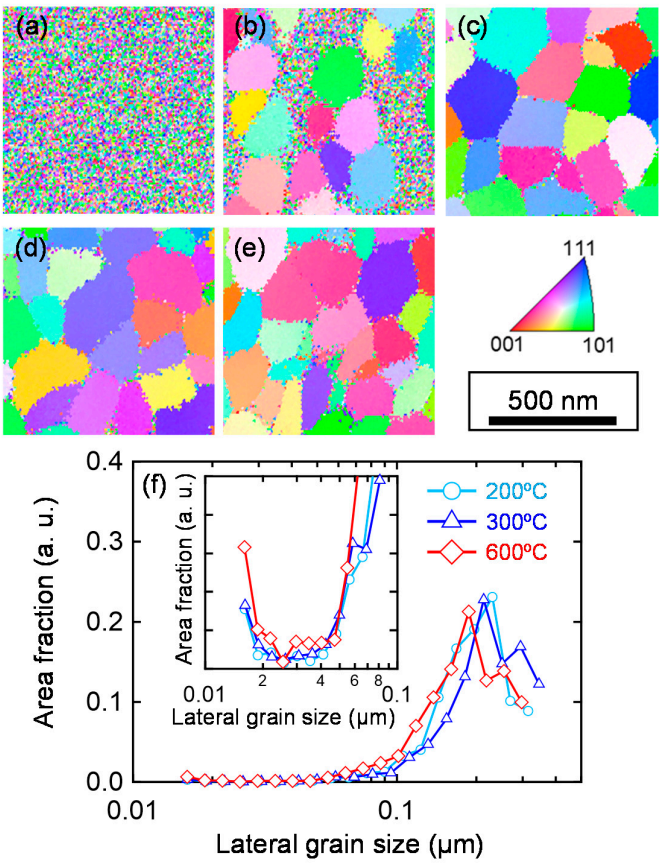

Figure 4. EBSD images of the (**a**) as-deposited, (**b**) 150 °C, (**c**) 200 °C, (**d**) 300 °C, and (**e**) 600 °C annealed In_2O_3:H films. (**f**) Area fraction of each grain size obtained from the In_2O_3:H films with various T_{ann} values. The inset shows a magnified view of the small area fraction at a small grain size.

To understand the mechanism of structural deterioration at the grain boundaries of In_2O_3:H films at $T_{ann} \geq 400$ °C, we performed TDS measurements. Figure 5 shows the TDS spectra of H_2, H_2O, O_2, and In for the In_2O_3 and In_2O_3:H films. We first note that H_2, O_2, and In desorption were negligible for both types of films, while the H_2O desorption was high for the In_2O_3:H film in particular. Large amounts of H_2O were desorbed at a stage temperature of 400–800 °C for the In_2O_3:H film (Figure 5b). The amount of hydrogen in the film was quantitatively evaluated using SIMS, and it was found that 2.6×10^{21} cm^{-3} of hydrogen remained in the film after SPC at 300 °C, which was one order of magnitude higher than that of the In_2O_3 film. The H_2O desorption temperature (400 °C) for the In_2O_3:H film corresponded well to a T_{ann} of 400 °C, at which the μ_H of the films started to degrade. During annealing at a T_{ann} of 400 °C and higher, H or –OH inside grains may migrate to grain boundaries and react with a neighboring H at the boundary, resulting in the generation of H_2O molecules. As a consequence, defects are formed at grain boundaries. In other words, the presence of H and/or –OH bonds in the In_2O_3:H film after SPC plays an important role in the passivation of defects, especially for grain boundaries. In general, the *SS* value of a TFT is strongly affected by defects near the semiconductor Fermi level [2,12]. We recently reported from hard X-ray photoelectron spectroscopy analysis that intentionally introduced hydrogen is effective in reducing defects near the Fermi level in amorphous IGZO [40–44]. The *SS* values of the In_2O_3:H TFTs, shown in Figure 2d, increased at a T_{ann} of 400 °C and higher, indicating defect creation. Thus, we believe that the H and/or –OH bonds remained in the films after SPC passivated the defects near the Fermi level, leading to the high μ_{FE} and steep *SS* values of the In_2O_3:H TFT annealed at 300 °C. Thus, it is worth noting that grain boundary scattering, which is a serious issue for polycrystalline Si TFTs, may not have a strong influence on the μ_{FE} of polycrystalline In_2O_3:H TFTs.

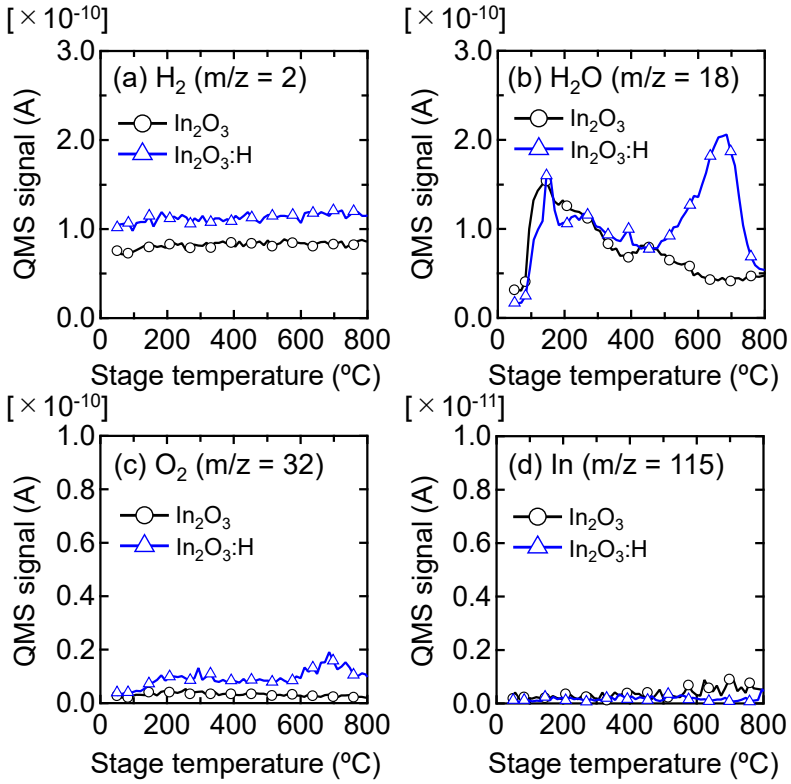

Figure 5. (**a**) H_2, (**b**) H_2O, (**c**) O_2, and (**d**) In desorption spectra from as-deposited In_2O_3 and In_2O_3:H films.

4. Conclusions

In summary, we investigated the effects of annealing temperature on the electron transport properties of In_2O_3:H films and TFTs. The changes in the electrical properties of the In_2O_3:H films were classified into the three following regions.

(I) When T_{ann} = 200 °C, μ_H increased by converting amorphous In_2O_3:H into a polycrystalline In_2O_3:H film with an increase in grain size.

(II) When T_{ann} = 250–350 °C, μ_H decreased with decreasing N_e. However, when μ_H exhibited low values, the medium-range ordering in the grains improved. The In_2O_3:H TFT annealed at 300 °C exhibited the best performance, with a μ_{FE} of 139.2 cm^2 V^{-1} s^{-1}.

(III) When $T_{ann} \geq$ 400 °C, although μ_H significantly decreased with constant or increasing N_e, the μ_{FE} of the TFTs was maintained at 94.6 cm^2 V^{-1} s^{-1}. The medium-range ordering of the In_2O_3:H network was improved by a T_{ann} of 600 °C, while a large amount of hydrogen was desorbed at 400–800 °C, resulting in defect creation at the grain boundaries. Thus, it was suggested that the hydrogen remaining in the film after SPC plays an important role in the passivation of electron traps, especially for the grain boundaries of the In_2O_3:H films, resulting in an enhancement of the μ_{FE}. We believe that the SPC-grown In_2O_3:H TFTs are promising candidates for use in future electronics applications.

Supplementary Materials: The following supporting information can be downloaded at: https://www.mdpi.com/article/10.3390/nano12172958/s1, Figure S1: Variations of transfer characteristics of the In_2O_3:H TFTs with channels annealed at various temperatures; Table S1: Summary of the TFT properties.

Author Contributions: Conceptualization, M.F. and Y.M.; Experimental work and fabrication of films and devices, Y.M.; characterization of films and devices, data analysis, Y.M., W.Y., T.I. and M.F.; design and fabrication of pulse-DC sputtering apparatus for film deposition and set up of the experimental environment for TFT fabrication and evaluation, W.Y.; writing—original draft preparation, Y.M.; writing—review and editing, W.Y., T.I. and M.F. All authors have read and agreed to the published version of the manuscript.

Funding: This work was partly supported by JSPS KAKENHI Grant No. 20K22415, No. 22K14303 and the Iketani Science and Technology Foundation No.0331062-A.

Institutional Review Board Statement: Not applicable.

Informed Consent Statement: Not applicable.

Data Availability Statement: The data are available on the request from corresponding author.

Acknowledgments: A part of this work was conducted in NAIST, supported by the Nanotechnology Platform Program (Synthesis of Molecules and Materials) of the Ministry of Education, Culture, Sports, Science and Technology (MEXT), Japan. The synchrotron radiation experiments were performed at the BL01B1 of SPring-8 with the approval of the Japan Synchrotron Radiation Research Institute (JASRI) (Proposal No. 2021B1455). The EBSD experiment was supported by the Next Generation Tatara Co-Creation Centre, Shimane University.

Conflicts of Interest: The authors declare no conflict of interest.

References

1. Nomura, K.; Ohta, H.; Takagi, A.; Kamiya, T.; Hirano, M.; Hosono, H. Room-temperature fabrication of transparent flexible thin-film transistors using amorphous oxide semiconductors. *Nature* **2004**, *432*, 488–492. [CrossRef] [PubMed]
2. Kamiya, T.; Hosono, H. Material characteristics and applications of transparent amorphous oxide semiconductors. *NPG Asia Mater.* **2010**, *2*, 15–22. [CrossRef]
3. Takeda, Y.; Aman, M.; Murashige, S.; Ito, K.; Ishida, I.; Matsukizono, H.; Makita, N. Automotive OLED display with high mobility top gate IGZO TFT backplane. *ITE Trans. Media Technol. Appl.* **2020**, *8*, 224–229. [CrossRef]
4. Kamiya, T.; Nomura, K.; Hosono, H. Origins of High Mobility and Low Operation Voltage of Amorphous Oxide TFTs: Electronic Structure, Electron Transport, Defects and Doping*. *J. Disp. Technol.* **2009**, *5*, 468–483. [CrossRef]
5. Kamiya, T.; Nomura, K.; Hosono, H. Present status of amorphous In–Ga–Zn–O thin-film transistors. *Sci. Technol. Adv. Mater.* **2010**, *11*, 044305. [CrossRef]
6. Ide, K.; Nomura, K.; Hosono, H.; Kamiya, T. Electronic Defects in Amorphous Oxide Semiconductors: A Review. *Phys. Status Solidi Appl. Mater. Sci.* **2019**, *216*, 1800372. [CrossRef]
7. Toda, T.; Tatsuoka, G.; Magari, Y.; Furuta, M. High-performance top-gate and self-aligned In–Ga–Zn–O thin-film transistor using coatable organic insulators fabricated at 150 °C. *IEEE Electron Device Lett.* **2016**, *37*, 1006–1009. [CrossRef]
8. Magari, Y.; Makino, H.; Furuta, M. Carrier generation mechanism and origin of subgap states in Ar- and He-plasma-treated In–Ga–Zn–O thin films. *ECS J. Solid State Sci. Technol.* **2017**, *6*, Q101–Q107. [CrossRef]

9. Magari, Y.; Furura, M. Effects of water and hydrogen introduction during In–Ga–Zn–O sputtering on the performance of low-temperature processed thin-film transistors. *Jpn. J. Appl. Phys.* **2021**, *60*, SBBM04. [CrossRef]
10. Magari, Y.; Aman, S.G.M.; Koretomo, D.; Masuda, K.; Shimpo, K.; Furura, M. Low-Temperature (150 °C) processed metal-semiconductor field-effect transistor with a hydrogenated In–Ga–Zn–O stacked channel. *Jpn. J. Appl. Phys.* **2020**, *59*, 2–7. [CrossRef]
11. Furuta, M.; Koretomo, D.; Magari, Y.; Aman, S.G.M.; Higashi, R.; Hamada, S. Heterojunction channel engineering to enhance performance and reliability of amorphous In–Ga–Zn–O thin-film transistors. *Jpn. J. Appl. Phys.* **2019**, *58*, 090604. [CrossRef]
12. Aman, S.G.M.; Koretomo, D.; Magari, Y.; Furuta, M. Influence of Deposition Temperature and Source Gas in PE-CVD for SiO_2 Passivation on Performance and Reliability of In–Ga–Zn–O Thin-Film Transistors. *IEEE Trans. Electron Devices* **2018**, *65*, 3257–3263. [CrossRef]
13. Ohshima, H. Value of LTPS: Present and future. *SID Symp. Dig. Tech. Pap.* **2014**, *45*, 75–78. [CrossRef]
14. Nomura, K.; Ohta, H.; Ueda, K.; Kamiya, T.; Hirano, M.; Hosono, H. Thin-film transistor fabricated in single-crystalline transparent oxide semiconductor. *Science* **2003**, *300*, 1269–1272. [CrossRef] [PubMed]
15. Aikawa, S.; Nabatame, T.; Tsukagoshi, K. Effects of dopants in InO_X-based amorphous oxide semiconductors for thin-film transistor applications. *Appl. Phys. Lett.* **2013**, *103*, 172105. [CrossRef]
16. Nakata, M.; Zhao, C.; Kanicki, J. DC Sputtered Amorphous In–Sn–Zn–O Thin-Film Transistors Electricalproperties and Stability. *Solid-State Electron.* **2016**, *116*, 22–29. [CrossRef]
17. Shiah, Y.S.; Sim, K.; Ueda, S.; Kim, J.; Hosono, H. Unintended Carbon-related Impurity and Negative Bias Instability in High-Mobility Oxide TFTs. *IEEE Electron Device Lett.* **2021**, *42*, 1319–1322. [CrossRef]
18. Koretomo, D.; Hashimoto, Y.; Hamada, S.; Miyanaga, M.; Furuta, M. Influence of a SiO_2 passivation on electrical properties and reliability of In–W–Zn–O thin-film transistor. *Jpn. J. Appl. Phys.* **2019**, *58*, 018003. [CrossRef]
19. Takahashi, T.; Fujii, M.N.; Miyanaga, R.; Miyanaga, M.; Ishikawa, Y.; Uraoka, Y. Unique degradation under AC stress in high-mobility amorphous In–W–Zn–O thin-film transistors. *Appl. Phys. Express* **2020**, *13*, 054003. [CrossRef]
20. Yang, J.H.; Choi, J.H.; Cho, S.H.; Pi, J.E.; Kim, H.O.; Hwang, C.S.; Park, K.; Yoo, S. Highly Stable AlInZnSnO and InZnO Double-Layer Oxide Thin-Film Transistors with Mobility over 50 cm^2/Vs for High-Speed Operation. *IEEE Electron Device Lett.* **2018**, *39*, 508–511. [CrossRef]
21. Choi, I.M.; Kim, M.J.; On, N.; Song, A.; Chung, K.B.; Jeong, H.; Park, J.K.; Jeong, J.K. Achieving High Mobility and Excellent Stability in Amorphous In–Ga–Zn–Sn–O Thin-Film Transistors. *IEEE Trans. Electron Devices* **2020**, *67*, 1014–1020. [CrossRef]
22. Lee, S.Y. Comprehensive Review on Amorphous Oxide Semiconductor Thin Film Transistor. *Trans. Electr. Electron. Mater.* **2020**, *21*, 235–248. [CrossRef]
23. Dhananjay; Chu, C.W. Realization of In_2O_3 thin film transistors through reactive evaporation process. *Appl. Phys. Lett.* **2007**, *91*, 132111. [CrossRef]
24. Hirao, T.; Furuta, M.; Furuta, H.; Matsuda, T.; Hiramatsu, T.; Hokari, H.; Yoshida, M.; Ishii, H.; Kakegawa, M. Novel top-gate zinc oxide thin-film transistors (ZnO TFTs) for AMLCDs. *J. Soc. Inf. Disp.* **2007**, *15*, 17–22. [CrossRef]
25. Presley, R.E.; Munsee, C.L.; Park, C.H.; Hong, D.; Wager, J.F.; Keszler, D.A. Tin oxide transparent thin-film transistors. *J. Phys. D Appl. Phys.* **2004**, *37*, 2810–2813. [CrossRef]
26. Higashi, S.; Ozaki, K.; Sakamoto, K.; Kano, Y.; Sameshima, T. Electrical properties of excimer-laser-crystallized lightly doped polycrystalline silicon films. *Jpn. J. Appl. Phys. Part 2 Lett.* **1999**, *38*, L857. [CrossRef]
27. Higashi, S.; Sugakawa, K.; Kaku, H.; Okada, T.; Miyazaki, S. Characterization of microcrystalline silicon thin film transistors fabricated by thermal plasma jet crystallization technique. *Jpn. J. Appl. Phys.* **2010**, *49*, 8–11. [CrossRef]
28. Koida, T.; Fujiwara, H.; Kondo, M. Hydrogen-doped In_2o_3 as high-mobility transparent conductive oxide. *Jpn. J. Appl. Phys. Part 2 Lett.* **2007**, *46*, 26–29. [CrossRef]
29. Magari, Y.; Kataoka, T.; Yeh, W.; Furura, M. High-Mobility Hydrogenated Polycrystalline In_2O_3 (In_2O_3:H) Thin-Film Transistors. *Nat. Commun.* **2022**, *13*, 1078. [CrossRef]
30. Weiher, R.L. Electrical properties of single crystals of indium oxide. *J. Appl. Phys.* **1962**, *33*, 2834–2839. [CrossRef]
31. Ravel, B.; Newville, M. Athena, Artemis, Hephaestus: Data analysis for X-ray absorption spectroscopy using IFEFFIT. *J. Synchrotron Radiat.* **2005**, *12*, 537–541. [CrossRef] [PubMed]
32. Fujiwara, H.; Kondo, M. Effects of carrier concentration on the dielectric function of ZnO:Ga and In_2O_3:Sn studied by spectroscopic ellipsometry: Analysis of free-carrier and band-edge absorption. *Phys. Rev. B Condens. Matter Mater. Phys.* **2005**, *71*, 075109. [CrossRef]
33. Koida, T.; Kondo, M.; Tsutsumi, K.; Sakaguchi, A.; Suzuki, M.; Fujiwara, H. Hydrogen-doped In_2O_3 transparent conducting oxide films prepared by solid-phase crystallization method. *J. Appl. Phys.* **2010**, *107*, 033514. [CrossRef]
34. Kataoka, T.; Magari, Y.; Makino, H.; Furuta, M. Nondegenerate Polycrystalline Hydrogen-Doped Indium Oxide (InO_X: H) Thin Films Formed by Low-Temperature Solid-Phase Crystallization for Thin Film Transistors. *Materials* **2022**, *15*, 187. [CrossRef]
35. Furuta, M.; Shimpo, K.; Kataoka, T.; Tanaka, D.; Matsumura, T.; Magari, Y.; Velichko, R.; Sasaki, D.; Kawashima, E.; Tsuruma, Y. High Mobility Hydrogenated Polycrystalline In–Ga–O (IGO:H) Thin-Film. *J. Soc. Inf. Disp.* **2021**, *52*, 69–72. [CrossRef]
36. Ellmer, K.; Vollweiler, G. Electrical transport parameters of heavily-doped zinc oxide and zinc magnesium oxide single and multilayer films heteroepitaxially grown on oxide single crystals. *Thin Solid Film.* **2006**, *496*, 104–111. [CrossRef]

37. Heald, S.; Alshammari, M.S.; Alfehaid, S.; Alotaibi, M.; Feng, Q.; Hakimi, A.M.H.R. XAFS study of metal-doped In_2O_3. *J. Phys. Conf. Ser.* **2013**, *430*, 8–12. [CrossRef]
38. Aliano, A.; Catellani, A.; Cicero, G. Characterization of amorphous In_2O_3: An ab initio molecular dynamics study. *Appl. Phys. Lett.* **2011**, *99*, 211913. [CrossRef]
39. Buchholz, D.B.; Ma, Q.; Alducin, D.; Ponce, A.; Jose-Yacaman, M.; Khanal, R.; Medvedeva, J.E.; Chang, R.P.H. The structure and properties of amorphous indium oxide. *Chem. Mater.* **2014**, *26*, 5401–5411. [CrossRef]
40. Magari, Y.; Aman, S.G.M.; Koretomo, D.; Masuda, K.; Shimpo, K.; Makino, H.; Kimura, M.; Furuta, M. Record-High-Performance Hydrogenated In-Ga-Zn-O Flexible Schottky Diodes. *ACS Appl. Mater. Interfaces* **2020**, *12*, 47739–47746. [CrossRef]
41. Aman, S.G.M.; Magari, Y.; Shimpo, K.; Hirota, Y.; Makino, H.; Koretomo, D.; Furuta, M. Low-Temperature (150 °C) Activation of Ar+O_2+H_2-Sputtered In–Ga–Zn–O for Thin-Film Transistors. *Appl. Phys. Express* **2018**, *11*, 081101. [CrossRef]
42. Koretomo, D.; Hamada, S.; Mori, M.; Magari, Y.; Furuta, M.; Furuta, M.; Furuta, M. Marked improvement in reliability of 150 °C processed IGZO thin-film transistors by applying hydrogenated IGZO as a channel material. *Appl. Phys. Express* **2020**, *13*, 076501. [CrossRef]
43. Magari, Y.; Aman, S.G.M.; Sasaki, D.; Furuta, M. Activation of igzo devices at 150 °C via reduction process using hydrogen gas during sputtering. *SID Symp. Dig. Tech. Pap.* **2021**, *52*, 1096–1099. [CrossRef]
44. Velichko, R.; Magari, Y. Defect Passivation and Carrier Reduction Mechanisms in Hydrogen-Doped In–Ga–Zn–O (IGZO:H) Films upon Low-Temperature Annealing for Flexible Device Applications. *Materials* **2022**, *15*, 334. [CrossRef] [PubMed]